

Automated Identification of the Tip of the Red Giant Branch in Globular Clusters with Gaia Data

Yi Yang¹, Zhenzhen Shao^{1,2,3}, Xiaofeng Wang⁴ and Xiaochen Zheng¹

¹ Department of Scientific Research, Beijing Planetarium, Beijing Academy of Science and Technology, Beijing 100044, China; *mgcyung@gmail.com*

² Institute for Frontiers in Astronomy and Astrophysics, Beijing Normal University, Beijing 102206, China; *201011161010@mail.bnu.edu.cn*

³ School of Physics and Astronomy, Beijing Normal University, Beijing 100875, China;

⁴ Physics Department, Tsinghua University, Beijing 100084, China; *wang_xf@mail.tsinghua.edu.cn*

Received 20xx month day; accepted 20xx month day

Abstract This study introduces an automated approach for identifying the tip of the red giant branch (TRGB) in globular clusters, combining astronomical data with algorithmic methods. Using a dataset of 160 globular clusters and Python scripts, we matched stellar sources with Gaia data. Our script generates color-magnitude diagrams (CMDs), and uses the local outlier factor (LOF) algorithm to remove outliers. Applying a second-degree polynomial to fit red giant branch (RGB), we identify the TRGB as the star closest to the fitted curve's endpoint. By this method, we expanded TRGB samples in globular clusters to 91 with newer observational data. Our results show a decreasing trend in I-band luminosity for metallicities greater than -1 , consistent with previous studies. The results show a robust trend fitting and the M_I of TRGB is about -4.02 with extremely low metallicity. Our approach enhances TRGB identification efficiency while providing valuable insights for developing automatic tools in astronomical data analysis.

Key words: methods: data analysis — stars: abundances — stars: general

1 INTRODUCTION

The tip of the red giant branch (TRGB) marks the maximum luminosity attained by stars as they evolve along the red giant branch (RGB) in the Hertzsprung-Russell diagram (HRD). Characterized by its consistent I-band absolute magnitude, the TRGB serves as a valuable standard candle for distance estimation in nearby galaxies (Freedman et al. 2019; Hoyt et al. 2021; Bellazzini et al. 2001; Rizzi et al. 2007; Sakai et al. 2000), with growing applications in Hubble constant measurements (Freedman 2021; Freedman et al. 2019; Yuan et al. 2019; Anand et al. 2021; Soltis et al. 2021). Previous investigations have revealed metallicity dependence of the TRGB's absolute magnitude. Studies by Salaris & Cassisi (1997) and Serenelli et al. (2017) established I-band luminosity-metallicity relationships through stellar evolution modeling, while Da Costa & Armandroff (1990) and Ferraro et al. (2000) examined relationships between each of bolometric magnitudes, color indices, bolometric corrections and metallicity. Building on this foundation, Bellazzini et al. (2001) and Jang & Lee (2017) developed empirical relations between I-band absolute magnitude and metallicity.

Current TRGB detection methodologies primarily employ edge detection algorithms and parametric fitting approaches. The Sobel filter method (McQuinn et al. 2017; Jang & Lee 2017; Scolnic et al. 2023) identifies luminosity function discontinuities through kernel-based gradient estimation, though its performance is sensitive to smoothing parameter optimization. Alternative techniques fit broken power-law models to the luminosity function (Li et al. 2023; Li & Beaton 2024), but these assume a single discontinuity in the RGB structure.

Globular clusters, provide an ideal environment for TRGB studies. Their color-magnitude diagrams (CMDs) typically encompass complete stellar evolutionary sequences from main sequence through red giant to horizontal branch stages. The near-uniform age and metallicity of cluster members - primary factors influencing TRGB luminosity - offer particularly favorable conditions for analysis. However, due to the limited number of RGB stars in individual clusters, conventional edge detection and parametric fitting approaches prove less effective for TRGB identification (Bellazzini et al. 2004).

TRGB corresponds to the theoretical evolutionary track of the RGB and exhibits the highest luminosity in globular clusters. Nevertheless, the conversion of luminosity to magnitude is influenced by effective temperature, surface gravity, metallicity, and bolometric correction, which means that the highest point of luminosity may not correspond to the brightest magnitude on a specific band in the CMD. Shao et al. (2025) referred that TRGB corresponds to the reddest star rather than brightest one in globular clusters.

Building on previous work, Shao et al. (2025) demonstrated that M_I remains nearly constant for $[\text{Fe}/\text{H}] < -1.2$ but decreases with higher metallicity, using TRGB stars identified through selection of the reddest star in $G_{\text{BP}}-G_{\text{RP}}$ versus G_{RP} diagrams from 33 Galactic globular clusters. However, this metallicity relation remains constrained by limited sample sizes in metal-rich regimes ($[\text{Fe}/\text{H}] > -1.2$).

Extending the reddest RGB selection method of Shao et al. (2025), we implement an automated pipeline incorporating algorithmic filtering, outlier removal, and curve fitting for TRGB identification. This automated approach enables efficient processing of extensive datasets while maintaining selection consistency, reducing manual intervention, and enhancing result reproducibility. By automating the identification of TRGB stars in globular clusters, the method can be used for TRGB studies in large scale data in CSST and JWST (Anand et al. 2024).

2 DATA

The data employed in this study derive from the globular cluster star catalog compiled by Vasiliev & Baumgardt (2021). This catalog, combined with contemporary algorithmic techniques, facilitates precise TRGB star determination within globular clusters. The primary data source encompasses 160 globular clusters, as detailed in Vasiliev & Baumgardt (2021). Rigorous quality control measures are employed to select stars with reliable astrometric parameters. These refined subsets were then used to ascertain cluster properties and individual stellar membership probabilities through a mixed modeling approach extensively described in Section 2 of their work.

To achieve comprehensive RGB source coverage, we initially set the membership probability threshold at 90%. Subsequently, to minimize non-member star inclusion, we increased the threshold to 99%. We conducted a comparison between 90% and 99% membership probability thresholds, finding that most stars removed during filtering resided in the main sequence as the threshold increased from 90% to 99%, with statistical impact on RGB star selection being negligible for over 95% of clusters. However, five clusters showed partial RGB star exclusion under the stricter 99% criterion. Therefore, we selected 99% as the membership probability threshold, excluding these clusters from our final sample to maintain high selection standards. This stringent criterion aims to achieve datasets containing only confirmed cluster members (Vasiliev & Baumgardt 2021).

To enhance photometric information, we cross-matched our data with the Gaia DR3 catalog (Gaia Collaboration et al. 2023). This process provided BP (G_{BP}) and RP (G_{RP}) magnitudes for sample stars, which offer crucial color information for analysis.

We further augmented our dataset by cross-matching with Stetson et al. (2019) and the SIMBAD astronomical database (Wenger et al. 2000). While most data originated from Stetson et al. (2019), we

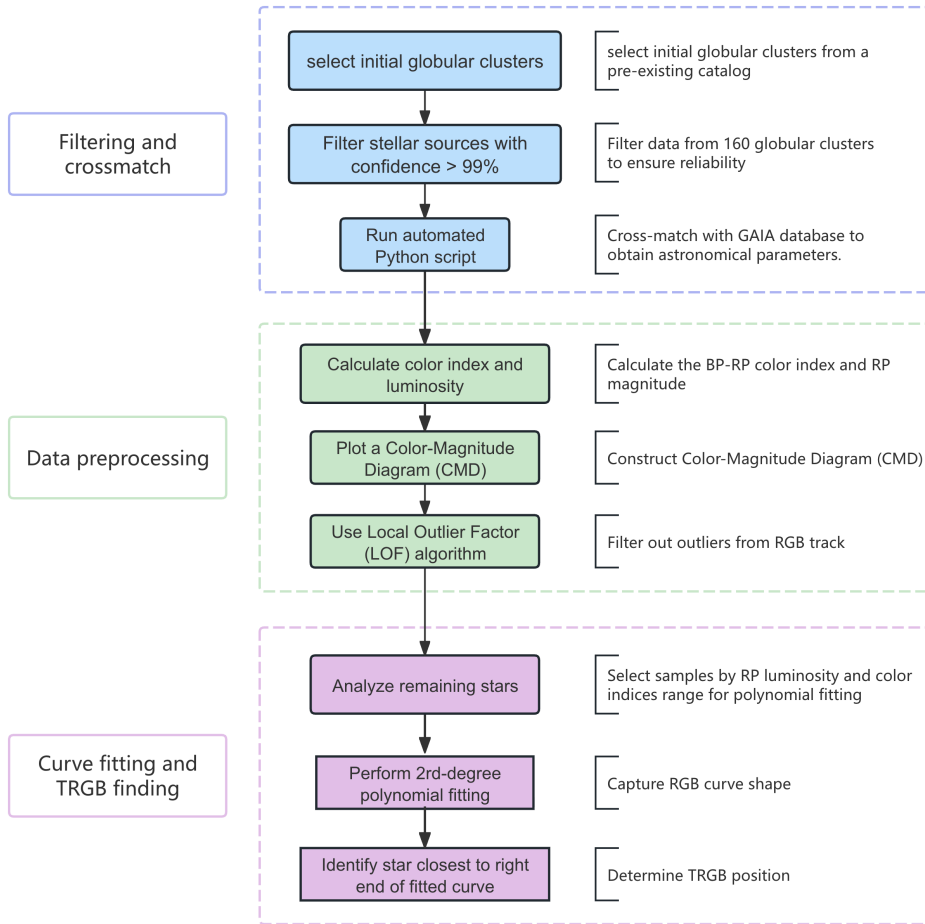


Fig. 1: Diagram of the TRGB seeking procedure, which includes data filtering and cross-referencing, data preprocessing, and curve fitting and TRGB finding.

queried SIMBAD for missing sources. This cross-matching process enabled retrieval of available V- and I-band magnitudes. Additionally, we supplemented these data through consultation of astronomical literature. When available, these magnitudes are crucial for accurate CMD construction and analysis.

3 METHOD AND DATA PROCESSING

As shown in Figure 1, our method primarily consists of three components: data filtering and cross-referencing, data preprocessing, and curve fitting and TRGB finding.

3.1 Filtering and crossmatching

As shown in Figure 1, the data filtering and cross-matching process comprises three key steps: cluster selection, stellar member selection, and Gaia database cross-matching.

We begin with an initial sample of 160 globular clusters from an existing catalog. Initial number of stars ranged from several dozen to several hundred thousand stars per cluster, depending on richness and observational coverage. We then filter stellar sources within these clusters by selecting those with

membership probabilities exceeding 99%, which minimized field star contamination while maintaining sufficient sample sizes (ranging from dozens to tens of thousands of stars per cluster) for reliable analysis. As shown in Figure 2, most stars (grey) removed during filtering resided in the main sequence as the threshold increased from 90% to 99%. Although globular clusters exhibit multiple stellar populations primarily affecting α -element abundances (C, N, O, etc.) (Leitinger et al. 2023), these variations negligibly impact [Fe/H] measurements, making metallicity determinations robust against population effects in our source selection.

Following this filtering step, we processed the data and performed a cross-match with the Gaia DR3 catalog using an automated Python script which utilizes *astropy* (The Astropy Collaboration et al. 2022) and *astroquery* (Ginsburg et al. 2019). This provides detailed astrometric parameters for each source, including high-precision positional, G magnitude, BP and RP magnitudes, parallax, and proper motions from Gaia (Gaia Collaboration et al. 2016, 2023), which are essential for further analysis in TRGB identification.

3.2 Data preprocessing

As shown in Figure 1, the data preprocessing stage involves three main operations: BP-RP color index calculation, CMD construction, and local outlier factor (LOF) filtering (Breunig et al. 2000).

Using Gaia data, we constructed CMDs for each cluster with BP-RP color indices and RP magnitudes which reveal stellar evolutionary stages. The RGB appears as a distinct sequence in these diagrams, with the TRGB positioned at its peak. As shown in Figure 2, these CMDs clearly delineate the red giant branch while visualizing stellar distributions, with typical ranges of $-1.0 < \text{BP}-\text{RP} < 5.0$ and $10 < \text{RP} < 22$ respectively.

After constructing the CMDs, we implemented a further culling step based on visual inspection of preliminary CMDs. We excluded globular clusters that either have a too small number of stars (such as NGC 6528), have a too small number of stars on RGB (such as NGC 6535), or have a dispersed RGB (such as NGC 6287) indicative of compromised data quality. This step ensured that subsequent analysis focused on clusters with sufficient data of adequate quality to allow for robust TRGB identification.

To improve TRGB identification accuracy, we apply the LOF algorithm to remove outliers from the RGB sequence. This unsupervised anomaly detection method identifies points that deviate significantly from their local neighborhood structure. Using parameters $n_neighbors=20$ and $contamination=0.005$, the filter effectively eliminates outliers which may have measurement errors while preserving the intrinsic RGB samples. The LOF algorithm removed 0-2.1% of outliers (average 0.4%) that deviated from CMD neighborhood structures, primarily eliminating potential measurement errors or non-member stars while preserving RGB morphology. As shown in Figure 2, these filtered outliers (green) typically occupied peripheral CMD regions, enhancing RGB clarity in the remaining sample (blue).

3.3 Curve fitting and TRGB identification

As depicted in Figure 1, the curve fitting and TRGB identification process involves three sequential steps: luminosity range-based sample selection, polynomial fitting, and TRGB determination.

After cleaning the data, we performed polynomial fit to stellar sources in each cluster. We first select stars with RP magnitudes no less than 3.0 mag of the brightest star on the red giant branch and with BP-RP color indices greater than 1.2 for polynomial fitting. This selection focuses on the luminous and red region of the RGB where the TRGB is expected to reside. A second-degree polynomial is then applied to fit on these selected samples using a HuberRegressor (Owen 2007), with BP-RP color index as the independent variable and RP magnitude as the dependent variable. This robust regression approach effectively balances curve representation and overfitting prevention, providing a reliable model of the RGB morphology.

The resulting polynomial curve effectively captured the overall trend of the red giant branch, which is a red curve in Figure 2. The TRGB candidate was identified as the star 'closest' to the right end of the fitted curve, corresponding to the reddest terminus of the red giant branch, as shown in Shao

et al. (2025). The closest means the weighted distance of each sample to the reddest terminus of the fitted curve, assigning a weight of 5.0 to the horizontal (BP–RP) axis and 1.0 to the vertical (RP) axis. This objective procedure ensures consistent identification of the RGB’s true apex while minimizing contamination from anomalous sources. As shown in Figure 2, the TRGB candidate was marked with a magenta triangle.

We examined our TRGB candidates and found that some were classified as long-period variable stars (LPVs) on SIMBAD. Anderson et al. (2024) show that TRGB candidates exhibit LPV characteristics, suggesting intrinsic brightness fluctuations in TRGB stars. As the primary source of contamination arises from asymptotic giant branch (AGB) stars. To mitigate this, we applied the empirical criterion that I-band variability amplitudes of AGB is larger than 0.14 mag (Lebzelter et al. 2005). We identified only one source exceeding the threshold on Gaia RP-band variability amplitudes¹ by cross math with a catalog covers magnitude variability of hundred million sources (Maíz Apellániz et al. 2023). The identified source was subsequently excluded from our final samples.

4 RESULTS AND DISCUSSION

After applying filtering, cross-matching, data preprocessing, curve fitting and TRGB identification, we ultimately obtained TRGBs for 94 globular clusters. We consider that they are the most possible TRGBs in these global clusters. Below we present results and discussion.

4.1 TRGB Results

By utilizing Gaia parallax-based distance calibrations for Galactic globular clusters from Vasiliev & Baumgardt (2021), combined with the color excess from Harris (2010) and the extinction law of Wang & Chen (2019), the absolute magnitudes of the TRGB in the V and I bands were determined. This enabled the derivation of the relationship between the TRGB’s absolute magnitude and the metallicity of globular clusters as cataloged in Harris (2010).

As shown in Figure 3, 34 samples (green dots) show consistency with the manual results (Shao et al. 2025), while 6 samples (red dots) display discrepancies. The TRGB points identified by our method closely match the manual selection, achieving an agreement of approximately 85%, thereby demonstrating the accuracy and reliability of our approach. Moreover, we extended 54 new samples (black dots).

The astrometric and photometric properties of 94 TRGB stars are summarized in Table 1. Specifically, the table presents the following information for each cluster: name, right ascension (RA) and declination (Dec) for J2000.0, distance, $E(B-V)$, $[Fe/H]$, M_I (absolute magnitude of I band), and Err_I (error of absolute magnitude of I band, which is calculated by distance error, photometric error, and extinction error).

Table 1: Catalogue of TRGBs in globular clusters.

Name	RA ($^{\circ}$)	DEC ($^{\circ}$)	Distance (kpc)	$E_{(B-V)}$ (mag)	$[Fe/H]$	M_I (mag)	Err_I (mag)
NGC 104	5.960	-72.097	4.521	0.04	-0.72	-3.978	0.026
NGC 288	13.171	-26.557	8.988	0.03	-1.32	-4.109	0.034
NGC 362	15.841	-70.905	8.829	0.05	-1.26	-3.704	0.031
NGC 1261	48.010	-55.180	16.4	0.01	-1.27	-4.002	0.025
NGC 1851	78.505	-40.034	11.951	0.02	-1.18	-3.908	0.024
NGC 1904	81.038	-24.571	13.078	0.01	-1.6	-3.948	0.030
NGC 2298*	102.248	-36.008	9.828	0.14	-1.92	-3.255	0.038

Continued on next page

¹ The I-band and RP wavelengths are close in proximity, allowing for the use of RP variability as an approximation for I-band variability.

Continued from previous page

Name	RA ($^{\circ}$)	DEC ($^{\circ}$)	Distance (kpc)	$E_{(B-V)}$ (mag)	[Fe/H]	M_I (mag)	Err_I (mag)
NGC 2808	138.084	-64.872	10.06	0.22	-1.14	-4.239	0.029
NGC 3201	154.746	-46.577	4.737	0.24	-1.59	-4.046	0.023
NGC 4590	189.852	-26.725	10.404	0.05	-2.23	-3.939	0.021
NGC 4833	194.771	-70.914	6.48	0.32	-1.85	-4.010	0.028
NGC 5024	198.189	18.191	18.498	0.02	-2.1	-4.085	0.022
NGC 5053*	199.051	17.772	17.537	0.01	-2.27	-3.399	0.029
NGC 5139	201.699	-47.491	5.426	0.12	-1.53	-4.028	0.019
NGC 5272	205.528	28.349	10.175	0.01	-1.5	-4.052	0.020
NGC 5466	211.557	28.503	16.12	0	-1.98	-4.008	0.025
NGC 5897	229.375	-21.035	12.549	0.09	-1.9	-3.934	0.051
NGC 5904	229.650	2.110	7.479	0.03	-1.29	-4.127	0.020
NGC 5927	232.003	-50.785	8.27	0.45	-0.49	-3.495	0.035
NGC 5986	236.483	-37.783	10.54	0.28	-1.59	-4.204	0.031
NGC 6093	244.273	-22.973	10.339	0.18	-1.75	-4.065	0.024
NGC 6101	246.564	-72.187	14.449	0.05	-1.98	-3.899	0.028
NGC 6121	245.860	-26.789	1.851	0.44	-1.16	-3.472	0.035
NGC 6144	246.803	-26.026	8.151	0.63	-1.76	-4.117	0.034
NGC 6171	248.130	-13.049	5.631	0.33	-1.02	-3.658	0.029
NGC 6205	250.424	36.447	7.419	0.02	-1.53	-4.027	0.024
NGC 6218	251.800	-1.922	5.109	0.19	-1.37	-3.900	0.021
NGC 6254	254.312	-4.097	5.067	0.28	-1.56	-4.063	0.027
NGC 6341	259.340	43.215	8.501	0.02	-2.31	-3.985	0.032
NGC 6352	261.505	-48.439	5.543	0.22	-0.64	-3.280	0.066
NGC 6362	262.963	-67.045	7.649	0.09	-0.99	-3.740	0.028
NGC 6366	261.893	-5.155	3.444	0.71	-0.82	-3.210	0.034
NGC 6397	265.084	-53.700	2.482	0.18	-2.02	-3.848	0.017
NGC 6541	272.089	-43.678	7.609	0.14	-1.81	-4.063	0.049
NGC 6656	279.034	-23.917	3.303	0.34	-1.7	-4.074	0.028
NGC 6723	284.923	-36.575	8.267	0.05	-1.1	-3.851	0.040
NGC 6752	287.739	-59.968	4.125	0.04	-1.54	-3.929	0.024
NGC 6779	289.152	30.146	10.43	0.26	-1.98	-3.817	0.030
NGC 6809	295.017	-30.972	5.348	0.08	-1.94	-3.935	0.022
NGC 6838	298.483	18.787	4.001	0.25	-0.78	-3.573	0.064
NGC 7078	322.509	12.189	10.709	0.1	-2.37	-4.087	0.020
NGC 7089	323.372	-0.799	11.693	0.06	-1.65	-3.964	0.021
NGC 7099	325.089	-23.164	8.458	0.03	-2.27	-4.186	0.024
Arp 2	292.183	-30.359	28.726	0.1	-1.75	-3.475	0.026
IC 4499	224.512	-82.196	18.891	0.23	-1.53	-4.215	0.030
Lynga 7	242.768	-55.315	7.899	0.73	-0.67	-3.870	0.044
NGC 2419	114.548	38.866	88.471	0.08	-2.15	-4.200	0.069
NGC 4372	186.642	-72.619	5.713	0.39	-2.17	-3.925	0.080
NGC 5286	206.620	-51.381	11.096	0.24	-1.69	-3.987	0.029
NGC 5634	217.408	-5.980	25.959	0.05	-1.88	-4.114	0.052
NGC 5694	219.897	-26.532	34.84	0.09	-1.98	-3.615	0.047
NGC 5824	225.972	-33.041	31.713	0.13	-1.91	-3.905	0.041
NGC 5946	233.865	-50.656	9.642	0.54	-1.29	-3.901	0.116
NGC 6139	246.924	-38.842	10.035	0.75	-1.65	-3.836	0.102
NGC 6229	251.725	47.560	30.106	0.01	-1.47	-3.860	0.213

Continued on next page

Continued from previous page

Name	RA ($^{\circ}$)	DEC ($^{\circ}$)	Distance (kpc)	$E_{(B-V)}$ (mag)	[Fe/H]	M_I (mag)	Err _I (mag)
NGC 6235	253.345	-22.136	11.937	0.31	-1.28	-3.815	0.075
NGC 6284	256.107	-24.770	14.208	0.28	-1.26	-3.993	0.071
NGC 6304	258.638	-29.430	6.152	0.54	-0.45	-3.301	0.052
NGC 6316	259.138	-28.133	11.152	0.54	-0.45	-3.457	0.081
NGC 6325	259.495	-23.782	7.533	0.91	-1.25	-3.753	0.097
NGC 6333	259.740	-18.572	8.3	0.38	-1.77	-3.784	0.048
NGC 6342	260.306	-19.572	8.013	0.46	-0.55	-3.678	0.069
NGC 6356	260.916	-17.812	15.656	0.28	-0.4	-3.783	0.129
NGC 6388	264.183	-44.787	11.171	0.37	-0.75	-3.316	0.086
NGC 6402	264.411	-3.267	9.144	0.6	-0.55	-4.075	0.130
NGC 6453	267.715	-34.610	10.07	0.64	-0.46	-3.855	0.056
NGC 6496	269.733	-44.239	9.641	0.15	-1.5	-3.450	0.034
NGC 6522	270.871	-30.047	7.295	0.48	-0.46	-3.525	0.096
NGC 6535	270.955	-0.285	6.363	0.34	-1.34	-3.873	0.042
NGC 6539	271.212	-7.571	8.165	1.02	-1.79	-3.765	0.107
NGC 6558	272.567	-31.750	7.474	0.44	-0.18	-3.829	0.082
NGC 6569 ^{†*}	273.439	-31.838	10.534	0.53	-0.76	-3.806	0.056
NGC 6584	274.648	-52.205	13.611	0.1	-1.5	-3.969	0.028
NGC 6624	275.943	-30.327	8.019	0.28	-0.44	-3.540	0.029
NGC 6626	276.165	-24.891	5.368	0.4	-1.32	-4.136	0.045
NGC 6637	277.840	-32.331	8.9	0.18	-0.64	-3.952	0.026
NGC 6638	277.741	-25.497	9.775	0.41	-0.95	-4.019	0.081
NGC 6652	278.924	-32.986	9.464	0.09	-0.81	-3.753	0.032
NGC 6681	280.816	-32.283	9.362	0.07	-1.62	-4.012	0.025
NGC 6712	283.337	-8.713	7.382	0.45	-1.02	-4.016	0.113
NGC 6717	283.797	-22.674	7.524	0.22	-1.26	-4.212	0.038
NGC 6760	287.809	1.039	8.411	0.77	-0.4	-3.612	0.112
NGC 6864	301.500	-21.920	20.517	0.16	-1.29	-4.156	0.047
NGC 6934	308.550	7.390	15.716	0.1	-1.47	-4.066	0.028
NGC 6981	313.370	-12.538	16.661	0.05	-1.42	-4.035	0.024
NGC 7006	315.372	16.180	39.318	0.05	-1.52	-3.977	0.031
NGC 7492	347.093	-15.628	24.39	0	-1.78	-3.595	0.051
Pal 4	172.311	28.971	101.39	0.01	-1.41	-3.630	0.055
Pal 8	280.385	-19.839	11.316	0.32	-0.37	-3.203	0.122
Pal 12	326.647	-21.239	18.494	0.02	-0.85	-3.426	0.035
Rup 106	189.652	-51.140	20.711	0.2	-1.68	-3.785	0.048
Terzan 3	247.094	-35.363	7.644	0.73	-0.74	-3.682	0.090
Terzan 7	289.413	-34.651	24.278	0.07	-0.32	-3.639	0.044
Terzan 8	295.500	-33.972	27.535	0.12	-2.16	-3.854	0.033

* denotes the TRGB not selected for the following analysis and

† denotes a possible AGB

4.2 Discussion

4.2.1 Relationship between TRGB absolute magnitude and metallicity

The absolute magnitude in the I band of the TRGB is a relatively stable constant, often used as a standard candle for distance measurement. However, stellar evolution theory reveals that the I band absolute magnitude depends on metallicity (Serenelli et al. 2017). At low metallicities, the I-band magnitude of

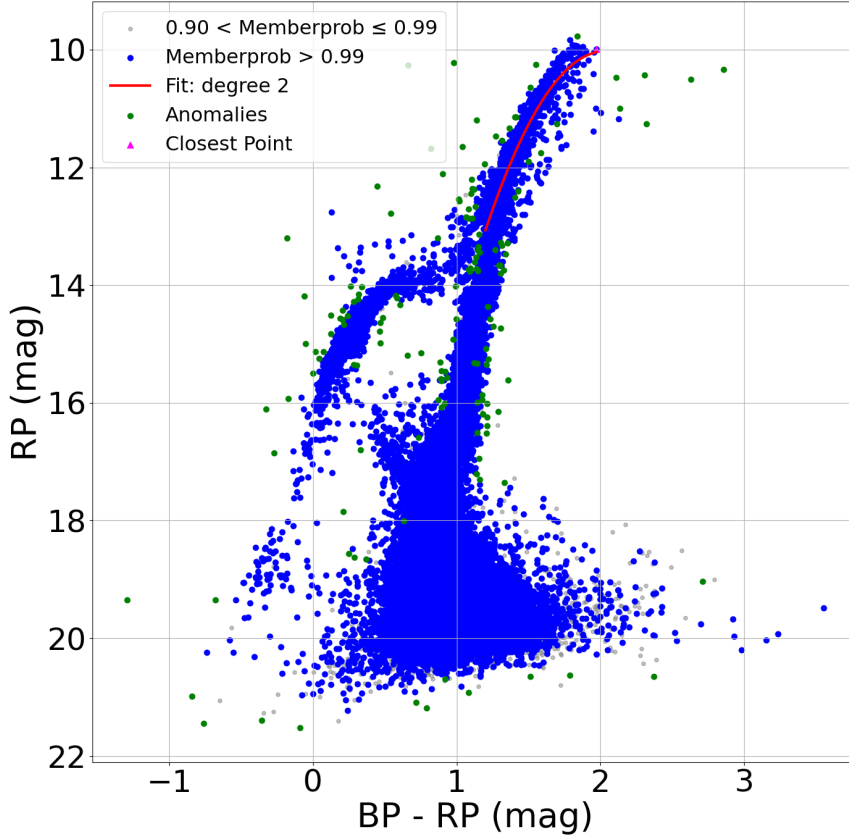


Fig. 2: Color-magnitude diagram for NGC 5139, showing sources with memberprob greater than 99% (blue dots), sources with memberprob in range from 90% to 99%, polynomial fit (red curve), outliers removed by LOF (green dots), and the identified TRGB candidate (magenta triangle).

the TRGB remains nearly constant. However, as metallicity increases, the I-band magnitude gradually fades. To quantify the effect of metallicity on the TRGB’s absolute magnitude, we plotted the relationship between TRGB metallicity and absolute magnitude using the previously calculated results. As shown in Figure 3, the analysis reveals a clear trend in I-band luminosity depending on metallicity.

For lower metallicities ($[\text{Fe}/\text{H}] < -1$), I-band luminosity remains relatively constant. At higher metallicities ($[\text{Fe}/\text{H}] > -1$), we observe a systematic I-band luminosity decrease. Our fitting yields an asymptotic constant -4.02 for absolute magnitude of I band in metal-poor region, consistent with previous studies (Freedman 2021; Freedman et al. 2019; Hoyt et al. 2021; Yuan et al. 2019; Anand et al. 2021). This consistency validates our algorithm’s effectiveness, with most of the automated selected TRGB samples matching manual selections from Shao et al. (2025). We excluded three samples (the globular clusters marked with an asterisk in Table 1) from the initial set of 94 TRGB sources: two beyond 3σ of our fit and one potential AGB star. The two deviant sources, also flagged by Shao et al. (2025), with a deviation from the trend line locating at the upper extremity, suggesting that these stars are generally warmer and may not have reached the TRGB stage in their evolution (Shao et al. 2025).

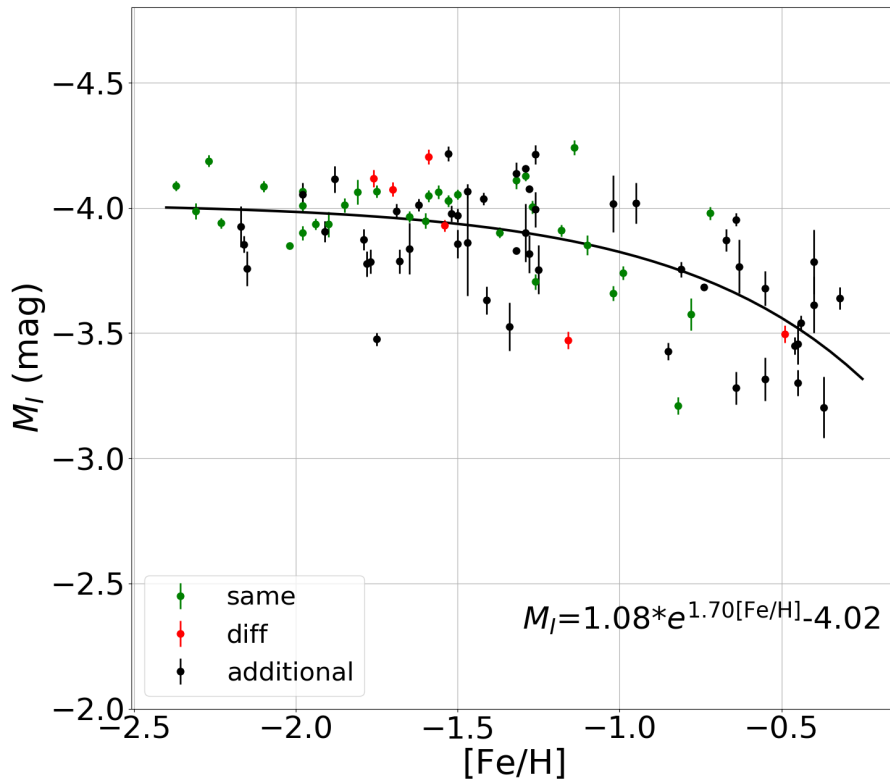


Fig. 3: Absolute magnitudes vs metallicity of TRGBs, showing TRGB samples identified consistently by both machine recognition and manual selection (green dots), inconsistent samples (red dots), and newly added star clusters (black triangles).

Previous investigations of TRGB metallicity dependence focused on relation between bolometric luminosity and $[\text{Fe}/\text{H}]$ using photographic photometry of about 6-8 Galactic globular clusters by selected the brightest RGB source as TRGB (Da Costa & Armandroff 1990; Ferraro et al. 2000). Building on this, Bellazzini et al. (2001) derived an M_I - $[\text{Fe}/\text{H}]$ relation by combining bolometric magnitude correlations from Ferraro et al. (2000) with color index and bolometric correction relations from Da Costa & Armandroff (1990). While these studies focused on bolometric luminosity correlations, their M_I - $[\text{Fe}/\text{H}]$ relationship remains a semi-empirical derivation. Our analysis benefits from Gaia DR3's (Gaia Collaboration et al. 2023) complete globular cluster photometry, covering wider metallicity ranges than previous studies. With 91 clusters analyzed - almost an order of magnitude improvement over typical samples of <10 clusters - we achieve richer metallicity coverage while maintaining astrometric precision for reliable TRGB detection.

To evaluate the systematic error of the method on TRGB absolute magnitude, we used its neighbour (the nearest star to each selected sample) in the CMD of each globular cluster to calculate its I-band absolute magnitude and compared it to the selected sample. As shown in Figure 4, we plotted the fitting curves for both the full sample and the binned sample along with the mean absolute magnitudes binned by $[\text{Fe}/\text{H}]$ with a size of 0.3 dex. Although the distribution between the reddest and their neighbour sources show a gap, the TRGB limiting magnitudes fitted for all sources become very close: -4.02 and

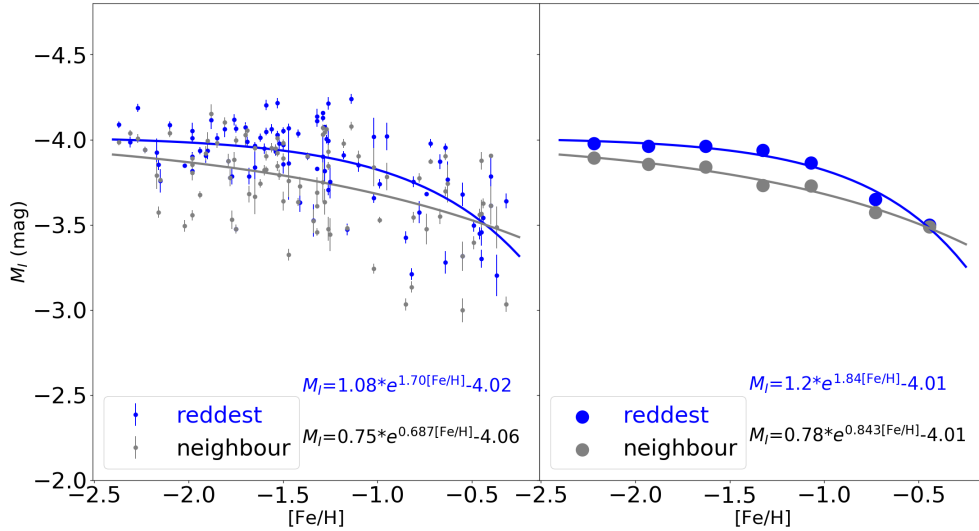


Fig. 4: Absolute magnitudes vs metallicity of TRGBs. Left panel: The blue dots represent data from selected samples, gray dots represent closest neighbors from each cluster’s selected sample, blue and gray lines denote the fitting curves respectively; Right panel: Same as left panel with M_I averaged in $[Fe/H]$ bins of 0.3 dex intervals.

−4.06 respectively, when metallicity approaches infinitesimal values. When fitting by bin, the derived TRGB limiting magnitudes are nearly identical at −4.01. By binning the fitting, the influence of the single TRGB metering error can be offset, and the fitting results are more consistent. This demonstrates that our fitting results are quite robust and consistent.

The TRGB limiting magnitudes difference of 0.04 between the reddest and their neighbour sources can be used as the systematic error of the method on TRGB absolute magnitude. This indicates that the results have good consistency, and the impact of error caused by the method is small.

Comparing the reddest and their neighbour sources reveals that when metallicity is low, the brightness of the reddest sources and the neighbour are similar in most clusters, with the neighbour being slightly dimmer which cause the neighbour fitting curve lower than the reddest one. However, at higher metallicities, especially above −0.6, the neighbour becomes brighter than the reddest source in some clusters. This aligns with the effect mentioned previously: as metallicity increases, there is a downward bending effect near the end of the red giant branches in CMDs, resulting in brighter neighbour sources. The disparity between the reddest and the neighbour sources primarily stems from the limited number of stars on the red giant branch and photometric errors. In clusters with sparser red giant branches, the brightness difference between the neighbour and the reddest one is larger than that in the dense clusters.

4.2.2 Relationship between TRGB color index and metallicity

As shown in Figure 5, by analyzing the TRGB results, we found a trend between metallicity ($[Fe/H]$) and color ($V - I$). The data suggests that as metallicity increases, the $V - I$ color index of the TRGB tends to increase. This indicates that metal-rich TRGB stars are generally redder than their metal-poor counterparts. This trend is consistent with stellar evolution theory that the extra metals in the atmospheres of metal-rich stars cause opacity in the convective atmosphere, making the star trap heat, expand and become cooler (Bressan et al. 2012). This is consistent with the trends marked as red x in Da Costa & Armandroff (1990). While the data in Da Costa & Armandroff (1990) is selected with M_I near −3 and our data is near −4, there is an upward shift as our samples is redder. The relationship between metallicity and color can be used to refine TRGB calibration and further distance measurements.

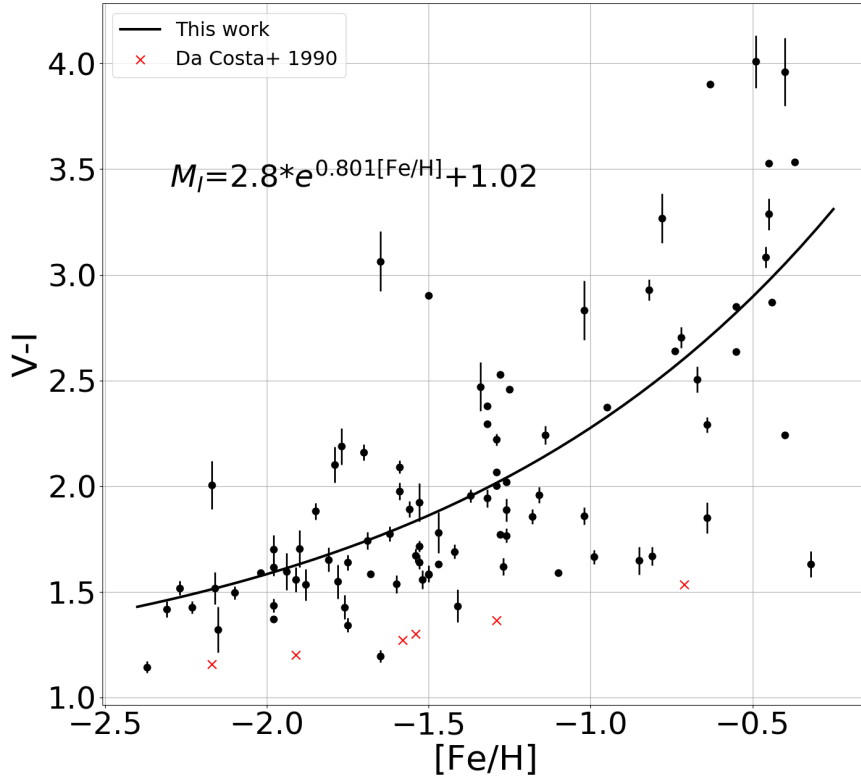


Fig. 5: Relationship between metallicity ($[\text{Fe}/\text{H}]$) and color index ($V - I$) of TRGB stars, with the fitted curve representing the trend. Red x markers denote samples in Da Costa & Armandroff (1990), and black dots denote our samples.

4.2.3 Performance and Applications of the Automated Method

This study successfully achieved the automatic identification and analysis of TRGB in globular clusters through the combination of automated scripts and algorithms. Compared to traditional manual methods, the automated approach not only improves efficiency but also aims to reduce the impact of artificial selection. Notably, our automated method expands the TRGB sample by over 100% (91 vs. 37), with a threefold increase in the metal-rich range ($-1 < [\text{Fe}/\text{H}] < 0$) where metallicity effects are most significant (Shao et al. 2025). The close agreement between our TRGB absolute magnitude–metallicity relation and previous results further validates the robustness and reliability of our approach.

Taking into account upcoming high-precision instruments such as JWST and CSST, while traditional manual identification methods are inefficient when dealing with the massive photometric datasets for star clusters in nearby galaxies like the Andromeda Galaxy (M31), the Large and Small Magellanic Clouds (LMC/SMC), the proposed automated TRGB identification method can address challenges. Our automated pipeline provides a scalable and objective framework capable of processing large volumes of high-resolution data with minimal human intervention. Therefore, this approach not only resolves the inefficiency and subjectivity of previous methods but also lays the foundation for automated, large-scale TRGB mapping in nearby galaxies.

However, this study also has some limitations. Firstly, the parameter selection of the LOF algorithm significantly affects the effectiveness of outlier identification, and further research is needed to optimize the parameters. Secondly, the determination of the TRGB depends on the accuracy of the fitted curve, and the choice of the fitting curve may affect the final result. Therefore, in future research, we plan to explore more advanced machine learning algorithms to improve the accuracy of TRGB identification. Additionally, expanding the sample size and exploring other data sources could further enhance the robustness and generalizability of our findings.

5 CONCLUSIONS

In conclusion, this study presents an automated methodology for identifying the TRGB in globular clusters. By integrating astronomical data with algorithmic techniques including data filtering and cross-matching, CMD construction, outlier removal, and second-degree polynomial fitting, we have developed an efficient and accurate process for TRGB identification. Finally, 91 TRGBs were identified from 160 global clusters, which extends samples in previous studies, especially on the high metallicity region. The results indicate a robust M_I fit around -4.02 at extremely low metallicities, with the I-band luminosity decreasing for metallicities above -1 . Our automated approach substantially enhances the efficiency of TRGB identification, enabling its effective application to large-scale datasets and forthcoming surveys such as CSST.

ACKNOWLEDGMENTS

This work is supported by the National Natural Science Foundation of China (No. 32300381, No. 12503027, No. 12303035, No. 12203007), Young Data Scientist Program of the China National Astronomical Data Center (No. NADC2025YDS-02), Innovation Ideas of Beijing Planetarium, Popular Science Project of Beijing Planetarium, China Manned Space Program with grant No. CMS-CSST-2025-A01, Beijing Natural Science Foundation (No. 1242016), and Talents Program (24CE-YS-08), Popular Science Project (24CD012), Innovation Project (24CD013), Mengya Program (BGS202203) of Beijing Academy of Science and Technology.

References

- Anand, G. S., Lee, J. C., Van Dyk, S. D., et al. 2021, *MNRAS*, 501, 3621
 Anand, G. S., Tully, R. B., Cohen, Y., et al. 2024, *ApJ*, 973, 83
 Anderson, R. I., Koblishke, N. W., & Eyer, L. 2024, *ApJL*, 963, L43
 Bellazzini, M., Ferraro, F. R., & Pancino, E. 2001, *ApJ*, 556, 635
 Bellazzini, M., Ferraro, F. R., Sollima, A., Pancino, E., & Origlia, L. 2004, *A&A*, 424, 199
 Bressan, A., Marigo, P., Girardi, L., et al. 2012, *MNRAS*, 427, 127
 Breunig, M. M., Krieger, H.-P., Ng, R. T., & Sander, J. 2000, *SIGMOD '00*, 93
 Da Costa, G. S., & Armandroff, T. E. 1990, *AJ*, 100
 Ferraro, F. R., Montegriffo, P., Origlia, L., & Fusi Pecci, F. 2000, *AJ*, 119, 1282
 Freedman, W. L. 2021, *ApJ*, 919, 16
 Freedman, W. L., Madore, B. F., Hatt, D., et al. 2019, *ApJ*, 882, 34
 Gaia Collaboration, Prusti, T., de Bruijne, J. H. J., et al. 2016, *A&A*, 595, A1
 Gaia Collaboration, Vallenari, A., Brown, A. G. A., et al. 2023, *A&A*, 674, A1
 Ginsburg, A., Sipőcz, B. M., Brasseur, C. E., et al. 2019, *AJ*, 157, 98
 Harris, W. E. 2010, arXiv:1012.3224
 Hoyt, T. J., Beaton, R. L., Freedman, W. L., et al. 2021, *ApJ*, 915, 34
 Jang, I. S., & Lee, M. G. 2017, *ApJ*, 835, 28
 Lebzelter, T., Wood, P. R., Hinkle, K. H., Joyce, R. R., & Fekel, F. C. 2005, *A&A*, 432, 207
 Leitinger, E., Baumgardt, H., Cabrera-Ziri, I., Hilker, M., & Pancino, E. 2023, *MNRAS*, 520, 1456
 Li, S., & Beaton, R. L. 2024, arXiv:2403.17048

- Li, S., Casertano, S., & Riess, A. G. 2023, *ApJ*, 950, 83
- Maíz Apellániz, J., Holgado, G., Pantaleoni González, M., & Caballero, J. A. 2023, *A&A*, 677, A137
- McQuinn, K. B. W., Boyer, M. L., Mitchell, M. B., et al. 2017, *AJ*, 834, 78
- Owen, A. B. 2007, *Contemporary Mathematics*, 443, 59
- Rizzi, L., Tully, R. B., Makarov, D., et al. 2007, *ApJ*, 661, 815
- Sakai, S., Mould, J. R., Hughes, S. M. G., et al. 2000, *ApJ*, 529, 698
- Salaris, M., & Cassisi, S. 1997, *MNRAS*, 289, 406
- Scolnic, D., Riess, A. G., Wu, J., et al. 2023, *ApJL*, 954, L31
- Serenelli, A., Weiss, A., Cassisi, S., Salaris, M., & Pietrinferni, A. 2017, *A&A*, 606, A33
- Shao, Z., Wang, S., Jiang, B., et al. 2025, *ApJ*, 980, 218
- Soltis, J., Casertano, S., & Riess, A. G. 2021, *ApJL*, 908, L5
- Stetson, P. B., Pancino, E., Zocchi, A., Sanna, N., & Monelli, M. 2019, *Mon Not R Astron Soc*, 485, 3042
- The Astropy Collaboration, Price-Whelan, A. M., Lim, P. L., et al. 2022, *ApJ*, 935, 167
- Vasiliev, E., & Baumgardt, H. 2021, *MNRAS*, 505, 5978
- Wang, S., & Chen, X. 2019, *ApJ*, 877, 116
- Wenger, M., Ochsenbein, F., Egret, D., et al. 2000, *A&AS*, 143, 9
- Yuan, W., Riess, A. G., Macri, L. M., Casertano, S., & Scolnic, D. M. 2019, *ApJ*, 886, 61